Optically enhanced organic phototransistors for adaptive image processing under complex light conditions

He Shao [a,b], Yu Ji [a], Ruiheng Wang [a], Jing Liu [a], Yueqing Li [a], Benxin Liu [a], Wen Li [a], Yannan Xie [a], Linghai Xie [a,*], Johnny C. Ho [b,*], Wei Huang [a,c], Haifeng Ling [a,*]

[a] State Key Laboratory of Organic Electronics and Information Displays & Institute of Advanced Materials (IAM), Nanjing University of Posts & Telecommunications (NJUPT), Nanjing 210023, China
[b] Department of Materials Science and Engineering, City University of Hong Kong, Kowloon 999077, Hong Kong SAR
[c] Frontiers Science Center for Flexible Electronics (FSCFE), MIIT Key Laboratory of Flexible Electronics (KLoFE), Northwestern Polytechnical University (NPU), Xi'an 710072, China

A B S T R A C T

Effectively handling massive information in complex lighting conditions is crucial for security-focused machine vision, as it relies on precise image feature detection and encryption/decryption to ensure integrity and confidentiality. Traditional hardware, primarily based on complementary metal-oxide-semiconductor (CMOS) technology, struggles with the complexity of processing tasks around the clock. To address this challenge, a ternary organic heterostructure visuomorphic phototransistor was tailored for adaptive critical image processing. The light coupling induced by the porous heterostructural layer enhances the light absorption efficiency by 2.5-fold. Our phototransistor exhibits bidirectional photoresponse across the visible and near-infrared (NIR) spectral regions, enabling adaptive edge detection in varying lighting conditions with precision above 85 %. The phototransistor array facilitates image encryption/decryption with a superior accuracy of 12 %/90 % compared to existing counterparts. This ternary organic hetero-integration combines multiple response modes, enabling compact and efficient critical feature processing.

1. Introduction

In recent years, artificial intelligence systems have assumed a pivotal role in diverse facets of daily life, such as intelligent homes, autopilot vehicles, and medical diagnosis, by facilitating image recognition and analysis [1–3]. However, the partitioning of memory and processing units in traditional von Neumann architecture has limited the speed and quality of data processing [4–6]. The efficient processing mode of the human visual system for image information can serve as a valuable reference [7]. Visual stimuli are adeptly captured by photoreceptors in the retina and rapidly transmitted to the visual cortex of the brain for expeditious and intricate processing (Fig. 1a) [8,9]. Inspired by human vision, visuomorphic devices are expected to represent an efficient paradigm to meet the requirements of processing complex image information [10,11]. Researchers have developed image visual chips based on silicon complementary metal-oxide-semiconductor (CMOS) technology [12–14]. These innovations continue to grapple with challenges from circuit complexity, high energy consumption, limited

compatibility and integration [15–17]. Therefore, there is an urgent necessity for novel hardware design and software processing approaches to simplify information volume and accelerate processing tasks [18,19].

Critical feature processing can simplify extensive tasks and improve processing efficiency. Focusing on extracting and identifying key features and structures contributes to optimizing and accelerating large-scale image processing [20–22]. However, considering data security issues, concealing critical features to enhance data confidentiality is also essential when handling critical data [23,24]. Therefore, in the face of massive and complex image information, focusing on critical information processing is imperative for expanding the functionality of visuomorphic devices [25]. In addition, it is worth noting that current visuomorphic devices mainly rely on visible light response and capture objects in bright environments for recognition. Broadening the photoresponse range and implementing multiple response modes enable them to adapt to more complex detection environments. Nevertheless, it is still a challenge to realize bidirectional modulation of the entire visible spectrum and NIR region for one hardware device, as it typically

manifests either a positive or negative response to a singular wavelength [26,27].

In this work, a ternary organic heterostructure phototransistor was constructed, comprising a donor-acceptor bulk-heterojunction (BHJ) structure, along with a *p*-type semiconductor layer, as shown in Fig. 1b. Notably, a three-dimensional tunable porous photosensitive layer is constructed by a phase separation process (Fig. 1c). The Finite-difference time domain (FDTD) simulation results substantiate the capability of the porous structure to enhance light absorption power by 2.5-fold (Fig. 1d). Additionally, this device concurrently manifests non-volatile positive photoconductance (PPC) and volatile negative photoconductance (NPC) with threshold-switching characteristics for both red, green, blue (RGB) and even near-infrared (NIR) spectra. This remarkable wide-spectrum bidirectional photoresponse facilitates adaptive edge detection with precision above 85 % in varying lighting conditions. Subsequently, the phototransistor arrays are innovatively used to encrypt and decrypt image data. The encryption and decryption of image data with remarkable accuracy of 12 % and 90 % signify data security assurance.

2. Results and discussion

The phototransistor based on BHJ/pentacene was constructed with highly doped silicon (Si) as the substrate pre-grown with a 300 nm-thick SiO_2 layer. Subsequently, a 30 nm-thick polystyrene (PS) was spin-coated onto the substrate. The BHJ consists of PM6:Y7-BO with a volume ratio of 1:1, which was then formed on PS. In addition, the additives

of 1,10-decanediol (DDO) and 1-chloronaphthalene (CN) were introduced to control the morphology of PM6 and Y7-BO, respectively. The chemical structures of PM6, Y7-BO, DDO, and CN are exhibited in Fig. S1. The additive contents of DDO and CN are confirmed to be 0.1 vol %, 0.25 vol%, 0.5 vol%, and 1 vol%, respectively, which are the volume ratio of PM6 and Y7-BO solution, respectively. According to previous reports, the addition of DDO improved the crystallinity of the polymer donor PM6, while the CN enhanced the ordered crystallite structure of acceptor Y7-BO molecule [28,29]. The crystallization properties of pristine PM6 and Y7-BO without any additives on PS can be revealed by atomic force microscopy (AFM) results. As shown in Fig. S2, a dense and flat film was obtained upon spin-coating pristine PM6 onto PS and subsequent annealing. With increasing content of DDO, there is a discernible augmentation in grain size within the PM6 film, consequently leading to a concomitant elevation in crystallinity. When the pristine Y7-BO was spin-coated onto PS, as shown in Fig. S3, the introduction of a certain amount of CN caused Y7-BO to aggregate more orderly and exhibit distinct borders. Fig. S4 shows the effect of DDO on the PM6/Y7-BO BHJ film. The noticeable crystallization and porous structures were still observed in the annealed film. However, these porous structures were disordered and had varying depths and diameters, which could affect the subsequent growth of pentacene and thus reduce device performance. In contrast, when CN was further introduced, the film exhibited more uniform pores with increased diameters. This indicates that the uniformly tunable porous structure of the film is due to the synergistic effect of the two additives in the BHJ. The morphological differences between BHJ with DDO and DDO/CN
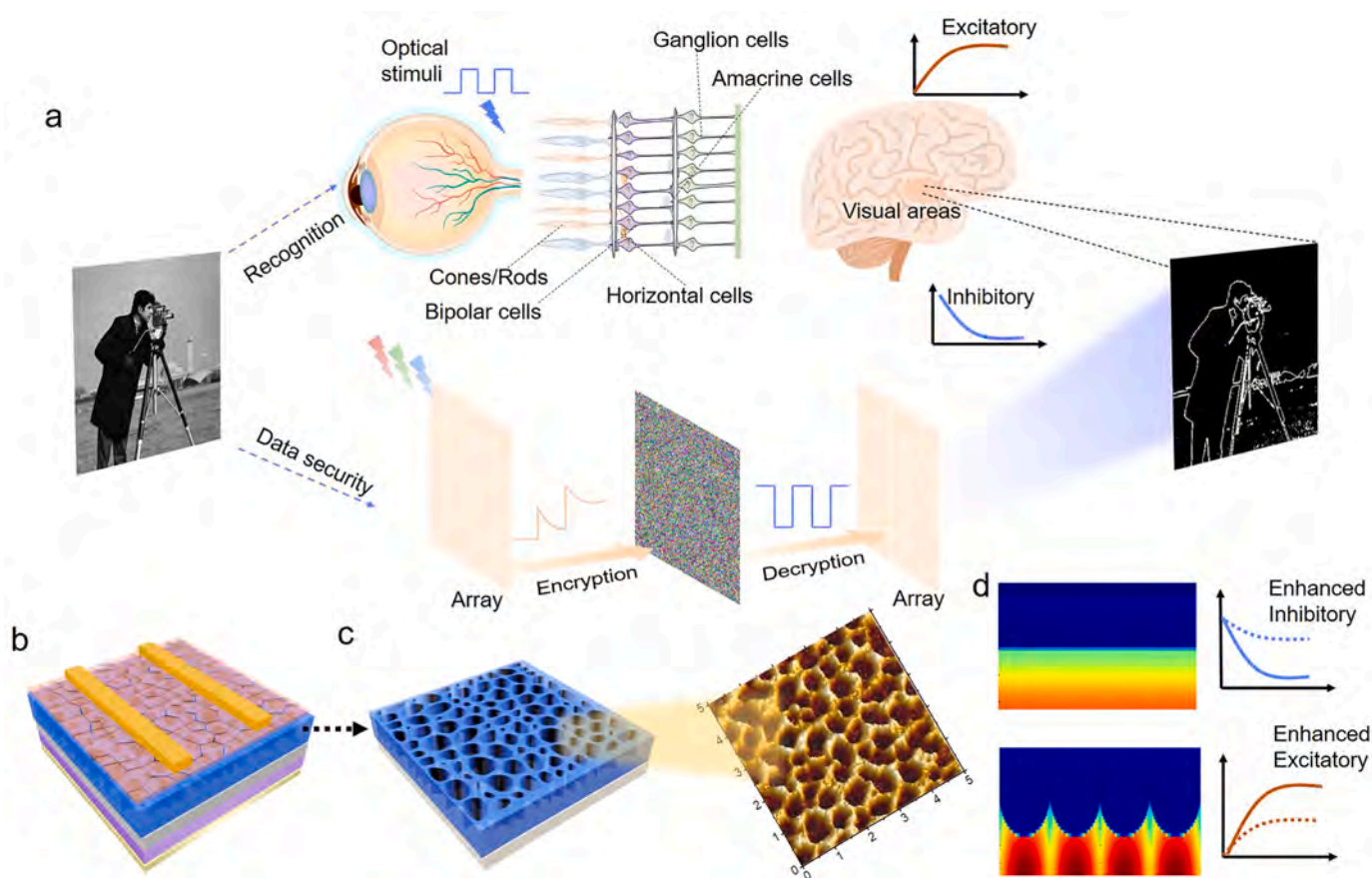

Fig. 1. (a) The schematic diagram of the visual system's processing and recognition of image information, as well as the process of image data security protection by visuomorphic devices. The excitatory and inhibitory represent the bipolar plasticity in the biological vision system. (b) The structure of the phototransistor with the BHJ/pentacene. The BHJ layer is composed of PM6, Y7-BO, CN and DDO. (c) The schematic diagram and the corresponding AFM image of the porous film. (d) The simulated light absorption intensity enhancement distribution of BHJ/pentacene film with and without pores along the direction above the surface of BHJ/pentacene film.

suggest that pore formation is induced by the excessive crystallization of PM6 and the subsequent ordered crystallization of Y7-BO [30–32].

The diameters and depths of pores within BHJ films, modulated by varying additive contents, are delineated in Fig. 2a-c, Figs. S5 and S6. The pertinent statistical distributions are depicted in Fig. S7. In the absence of additives, the resulting BHJ film displays a planar morphology. Conversely, upon introducing 0.1 vol% additives, discernible pores within the BHJ film become apparent. Notably, both the diameters and depths of these pores show augmentation as the additive contents escalated from 0.1 vol% to 1 vol%. Specifically, the respective average pore diameters were confirmed to be 150, 320, 420, and 520 nm for additive contents of 0.1 vol%, 0.25 vol%, 0.5 vol%, and 1 vol%. This trend indicates a direct correlation between the additive concentration and pore size, with higher additive contents leading to larger pore diameters. Correspondingly, these pores' mean depths were determined to be 15, 22, 45, and 70 nm, reflecting a similar trend where increased additive concentration results in deeper pores. The controlled modulation of pore dimensions through additive concentration highlights the tunability of the BHJ film's morphological properties, which could be pivotal for optimizing the film's performance in various applications. To ascertain that the observed pore formation stemmed from the enhanced aggregation of PM6 and ordered crystallization of Y7-BO facilitated by the additives, dynamic X-ray photoelectron spectroscopy (DXPS) was employed for a comprehensive analysis of BHJ films across varying additive contents. Fig. 2d-f elucidate the N 1 s depth profiling

images characteristic of the BHJ film. Notably, the N 1 s peak can be observed when the combined energy approaches 399.1 eV, where the color intensity is related to the magnitude of the peak signal [33]. Nitrogen serves as the discernible constituent of Y7-BO, thereby providing valuable insights into the spatial distribution and enrichment levels of Y7-BO across varied film depths. The additive-free BHJ film exhibits consistent N 1 s peak intensities across disparate etching depths, thereby corroborating the uniform dispersion of Y7-BO throughout the BHJ film. Conversely, a discernible attenuation in N 1 s signal intensity is observed in BHJ films incorporating additive contents of 0.1 vol% and 0.5 vol% as the etching process advanced, indicative of a pronounced accumulation of Y7-BO predominantly at the film's upper region. Consequently, incorporating additives within BHJ films engenders a heightened vertical phase segregation propensity. This phase separation optimizes the charge separation and transport mechanisms in phototransistors. The vertical phase segregation enhances charge separation efficiency by concentrating photon absorption and electron-hole pair generation in the acceptor region, thereby reducing recombination probability [34]. Additionally, vertical phase separation minimizes donor-acceptor mixing within the same plane, reducing defects and trap states that typically cause charge recombination and transport losses [35]. This leads to more complete and continuous transport pathways, thereby enhancing charge transport speed and efficiency [36,37].

Furthermore, the regional molecular ordering and orientation of Y7-BO and Y7-BO/CN in films were tested by grazing incidence wide-angle
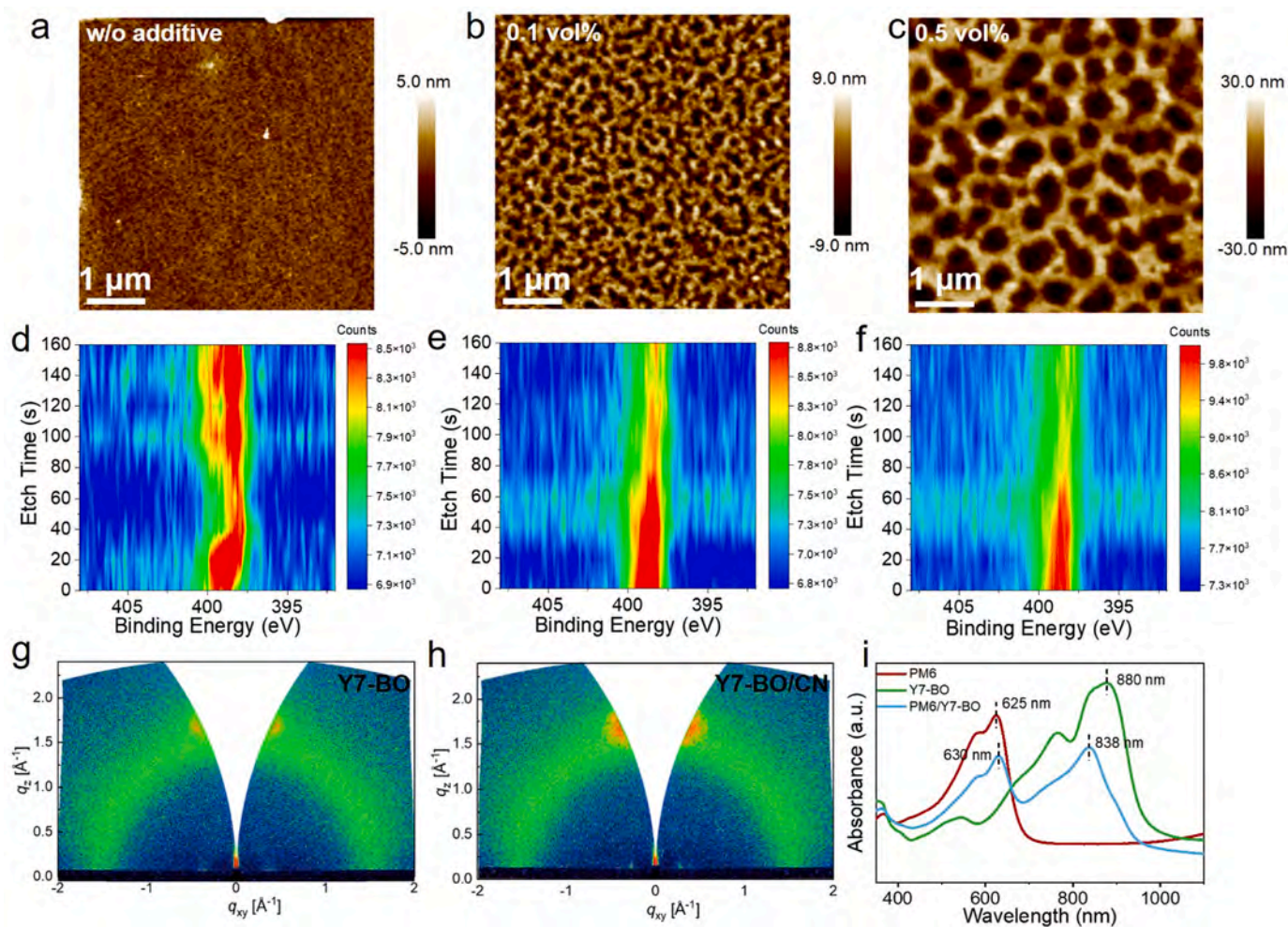

Fig. 2. (a-c) The AFM images of BHJ film without additives and with different additive contents of 0.1 vol% and 0.5 vol%. (d-f) DXPS spectra of BHJ film without additives and with different additive contents of 0.1 vol% and 0.5 vol%. (g-h) 2D grazing incidence wide-angle X-ray scattering (GIWAXS) image of Y7-BO without and with CN. (i) The absorption spectra of PM6, Y7-BO, and PM6/Y7-BO composite film.

X-ray scattering (GIWAXS), as shown in Fig. 2 g and 2 h. The corresponding data is carried out and shown in Table S1. The Y7-BO neat films without CN on PS shows a π–π stacking peak at 1.734 Å^{-1} in the out-of-plane (OOP) direction and major lamellae stacking peaks at 0.272 Å^{-1} in the in-plane (IP) direction, which is assigned to (110) lattice plane, determined from single crystal data previously reported [38,39]. For Y7-BO with CN, Fig. 2 h obviously shows that the orientation of Y7-BO is enhanced after the addition of CN, and the stacking peak in OOP and IP direction shows a slight position change compared to pristine Y7-BO. The same phenomenon is observed in PM6/Y7-BO films. As shown in Fig. S8, the stacking peaks in both IP and OOP directions increase after introducing CN compared with the film without
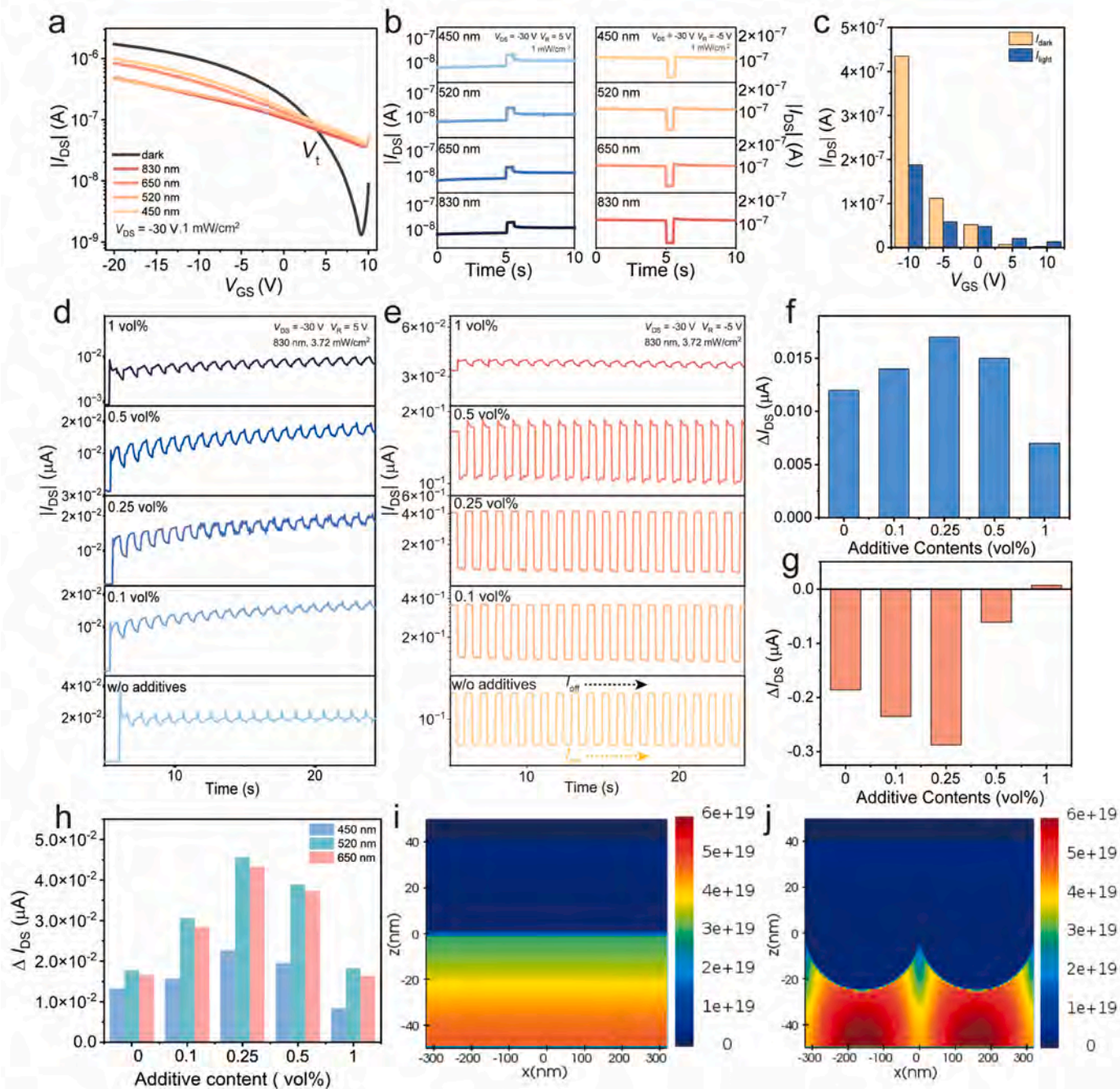

Fig. 3. (a) Transfer characteristics of the phototransistor without additives, captured under both dark conditions and illuminations with wavelengths of 450, 520, 650, and 830 nm. The incident light intensity is maintained at 1 mW/cm^2. (b) PPC and NPC response behaviors exhibited by the phototransistor without additives when exposed to light at wavelengths of 450, 520, 650, and 830 nm. (c) The statistical data of I_{DS} response of additive-free phototransistors when subjected to 830 nm light illumination at varying reading voltages. (d-e) Continuous I_{DS} responses of phototransistors with varied additive contents when stimulated by 830 nm light pulses under reading voltages of 5 V and −5 V, respectively (t_d = 0.5 s, Δt = 0.5 s, light intensity: 3.72 mW/cm^2). (f-g) The statistical data of ΔI_{DS} for the phototransistors with distinct additive contents, exposed to an 830 nm light pulses at an intensity of 1 mW/cm^2, recorded at reading voltages of 5 V and −5 V respectively. (h) The statistical data of ΔI_{DS} for the phototransistor with distinct additive contents, exposed to 450, 520, and 650 nm light at an intensity of 1 mW/cm^2, recorded at V_R of 5 V. (i-j) Simulated light absorption enhancement distributions for the BHJ/pentacene composite film within devices based on the BHJ film, both in its pristine form and with an additive content of 0.25 vol%.

additives. These results indicate that more substantial and more orderly crystallinity exists in Y7-BO with CN [40,41]. The absorption spectra in Fig. 2i also illustrate the crystallization and aggregation characteristics of PM6 and Y7-BO. For the BHJ film without additives, the characteristic peak of PM6 at 630 nm exhibits a red shift compared to that in the pristine PM6 film at 625 nm. The characteristic peak of Y7-BO at 838 nm shows a blue shift relative to the pristine Y7-BO film at 880 nm, substantiating the presence of intermolecular interactions between PM6 and Y7-BO [42]. The complementary absorption characteristics of PM6 and Y7-BO markedly enhance the device's overall performance. PM6 synergizes with Y7-BO can absorb the whole visible and NIR light. This pairing creates a synergistic effect that significantly boosts the phototransistor's efficiency and sensitivity. The donor-acceptor combination of PM6 and Y7-BO effectively mitigates defect issues commonly associated with traditional heterojunctions, resulting in improved charge separation and transport efficiency [43,44]. This combination minimizes recombination losses and maximizes the photocurrent, leading to remarkable performance in phototransistor applications. Subsequently, the phototransistor was constructed with a ternary heterostructure of BHJ/pentacene. Fig. S9 and S10 investigate the morphology of pentacene deposited on BHJ. Initially, when a 2 nm layer of pentacene was deposited on BHJ, the pentacene grains exhibited a loose and disordered state in films without pores. However, with a gradual increase in the contents of additives for BHJ film, the pentacene grains exhibited continuous growth along the Y7-BO, specifically along the edges of pores. When the pentacene thickness reaches 50 nm, the pentacene grains on the BHJ films, without and with 0.1 vol% additives, are uniformly distributed and densely packed. However, with additive contents of 0.25 vol%, 0.5 vol%, and 1 vol%, the pentacene grains infiltrated numerous pores, resulting in an uneven morphology of the pentacene film.

The electrical characteristics of the phototransistor are further investigated. Fig. 3a and Fig. S11 illustrate the transfer curves of the device constructed from BHJ/pentacene without additives and with different additive contents under both dark conditions and varying light illuminations with different wavelengths. The device without additives shows a typical p-type behavior and a current ratio of over 10^3 for dark conditions. Under light illumination, the photoresponse transitions from NPC to PPC by applying gate voltage. The signal reverses around $V_{GS} = 4$ V (defined as V_t), where the cross point is between the transfer characteristic curves under dark and illumination. The transformation of photoresponse characteristics under different gate reading voltages (V_R) is shown in Fig. 3b. For the reading voltage of 5 V, the device's photocurrent shows a positive response when the light is turned on. After the light is turned off, the photocurrent decays to a new equilibrium state higher than the initial resting state instead of disappearing completely, thus manifesting non-volatile characteristics. On the contrary, Under the reading voltage of −5 V, the device exhibits negative response and threshold switching characteristics, with the peak current lower than the initial resting state, and the photocurrent recovers quickly after the stimulation is completed. Fig. 3c and Fig. S12 show the photocurrent variation of the device at different reading voltages with the stimulation under 830 nm light (1 mW/cm², 0.5 s). As the reading voltage of positive and negative V_{GS} increases, the variation in current becomes more significant. Therefore, in order to minimize the impact of electron programming from V_{GS} on the current of the device, we selected a reading voltage of ±5 V based on the signal reverses of current in the transfer curve to further investigate PPC and NPC behavior. Additionally, the transfer characteristics presented in Fig. S11 demonstrate that devices with additive contents of 0.1 vol%, 0.25 vol%, and 0.5 vol% exhibit both positive and negative current changes at different V_{GS} when exposed to light. When the additive content reaches 1 vol%, the transfer curve shifts to the positive V_{GS} direction after light illumination, due to the excessive porosity affecting the continuity of the pentacene layer. The distinct photocurrent observed at different V_{GS} values is also supported by the typical output curve obtained under both dark and light

conditions. Fig. S13 and S14 demonstrate that for $V_{GS} < 0$, the I_{DS} under light illumination was lower compared to the dark condition, indicating a negative photoresponse. Conversely, for $V_{GS} > 0$, the I_{DS} under light illumination surpasses that observed in the dark, exhibiting a positive photoresponse. These results show that the polarity of the photoresponse of the device is affected by the reading voltage, which is consistent with the results of the transfer characteristic curves.

The phenomenon of consecutive photoconductance was subsequently observed by stimulating with multiple light pulses. Figs. 3d and 3e illustrate the photoresponse of devices based on BHJ/pentacene with varying additive contents in BHJ film under consecutive 830 nm light pulsed stimulation (3.72 mW/cm², $t_d = 0.5$ s, $\Delta t = 0.5$ s). Similarly, at a reading voltage of 5 V, an increase in light pulses results in a progressive rise in I_{DS}, suggesting consistent positive photoconductance. In contrast, under a reading voltage of −5 V, the device demonstrates a negative and volatile photoresponse. Notably, with a progressive increase in light pulses, substantial and sustained variations in photoconductance are absent, elucidating a characteristic threshold-switching behavior. It is significant to note that with an additive content of 1 vol%, all devices exhibit a positive photoresponse attributed to the discontinuous growth of pentacene. Fig. 3f-g and Fig. S15 illustrate the ΔI_{DS} relative to the resting state after applying an 830 nm light pulse with the intensity of 1 mW/cm². Both PPC and NPC behaviors demonstrate the most significant ΔI_{DS} at an additive content of 0.25 vol%. Fig. 3h and Fig. S16 show the ΔI_{DS} for devices with different additive contents under stimulations of distinct visible light wavelengths (450, 520, and 650 nm) with the intensity of 1 mW/cm². It also indicates that the device with 0.25 vol% additives exhibits the most significant ΔI_{DS} when subjected to visible light stimuli.

The observed variation in ΔI_{DS} can be attributed to diverse light-harvesting efficiencies of external light arising from variations in pore diameters and depths caused by different additive contents. It can be further validated through FDTD simulation modeling. Figs. 3i and 3j show the spatial profiles of the light absorption per unit volume with respect to the xz-plane at 830 nm for the flat interface between BHJ and pentacene. When constructing the model, we set the diameter of the pore in the BHJ model to 320 nm and the depth to 22 nm, which is consistent with the morphology of the 0.25 vol% additive BHJ films. The ratio of the absorbed power per unit volume (P_{abs}) of the porous structure to the planar structure is equal to the ratio of the square of the average intensity of electric field (E) [45]. According to the simulation results of Figs. 3i and 3j, the P_{abs} are increased by 2.5-fold by porous structure. The spatial distributions of light absorption at 450, 520, and 650 nm are illustrated in Fig. S17. Similarly, relative to a flat interface, the porous structure amplifies visible light absorption. Following this, the influence of varying pore sizes on light absorption density is similarly investigated. As illustrated in Fig. S18, under 830 nm light incidence, the absorption density with the pore diameter of 320 nm (0.25 vol%) was higher than that of 150 nm (0.1 vol%), consistent with the results reflected in the device's photocurrent.

To further clarify the positive and negative photoconductive behaviors observed under different reading voltages in the device, the energy level of the phototransistor-based BHJ/pentacene is illustrated in Fig. 4a. It indicates that pentacene forms a heterostructure with BHJ. Therefore, under illumination conditions, electrons and holes generated within the BHJ are simultaneously influenced by both the voltage applied on the gate and the energy barrier of pentacene. When $V_{GS} > V_t$, upon absorption of external light by the BHJ, the photo-generated excitons diffuse to the D/A interface, and the energy offsets between PM6 and Y7-BO lead to dissociation of the strongly bonded Frenkel excitons [46,47]. Under the influence of the electric field, electrons migrate towards the gate and are ultimately trapped by the PS. The resultant built-in electric field induces an accumulation of holes in the BHJ, leading to an increase in current and exhibiting non-volatile characteristics (Fig. 4b). Conversely, When $V_{GS} < V_t$, electron-hole pairs dissociate at the D-A interface, with holes entering into the pentacene due to the
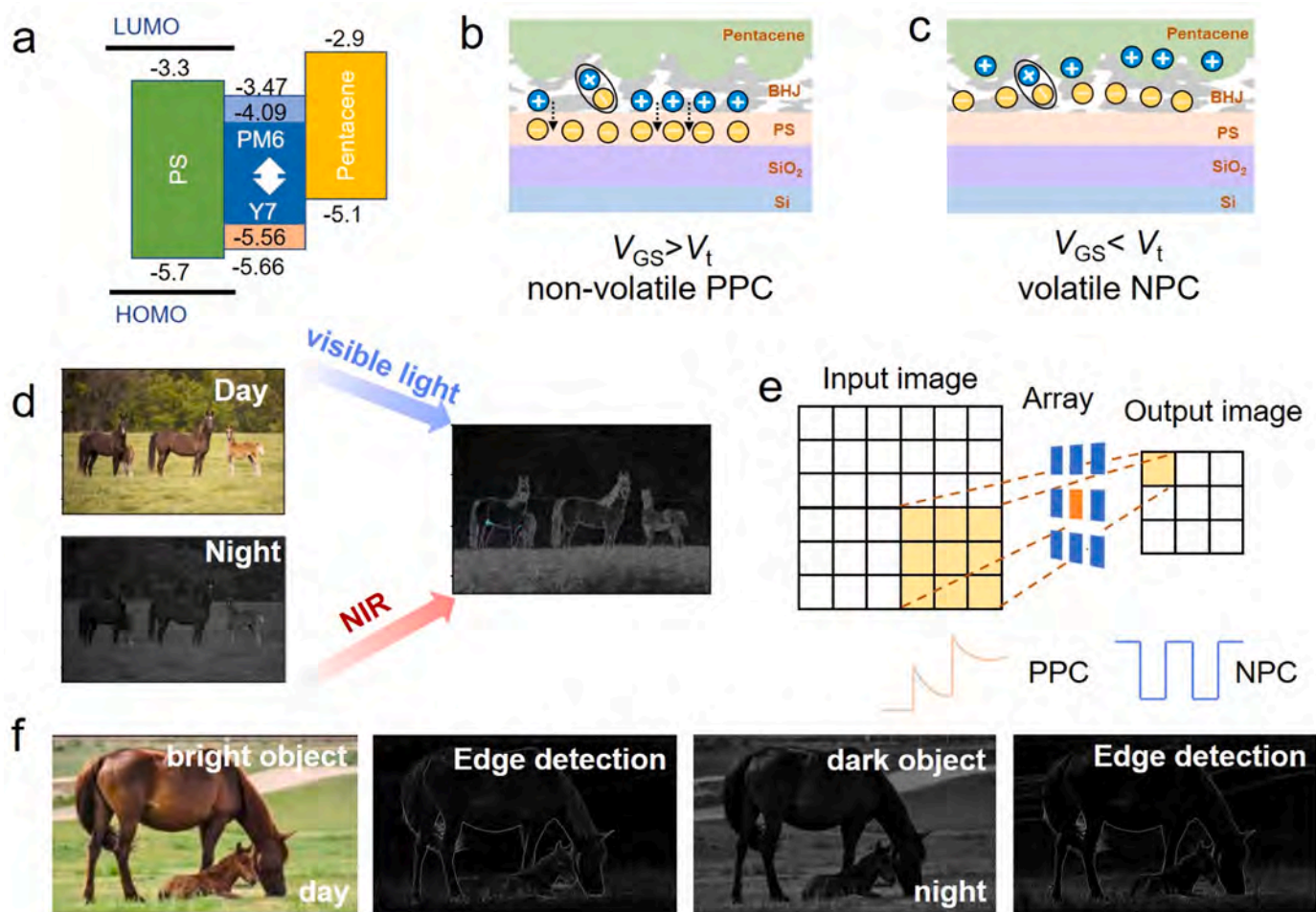
Fig. 4. (a) Schematic diagram of energy level diagram of the photonic synapse. The working mechanism of the device under (b) V_R of 5 V with non-volatile PPC behavior and (c) V_R of -5 V with volatile NPC behavior. (d) Schematic diagram of image edge detection process for day and night, respectively. (e) Schematic principle of the phototransistor array to achieve image processing. (f) The edge detection of objects in both bright and dark conditions realized by the response of phototransistors to visible and NIR light.

potential barrier energy levels. The excess electrons are left in the BHJ, causing a decreasing current. Under the driving force of the gate voltage, the holes quickly recombine with electrons within the BHJ. Consequently, the device manifests volatile properties (Fig. 4c).

The transition in the behaviors of PPC and NPC can be further substantiated by examining the individual charge transfer behaviors of devices based on PM6 and Y7-BO. The device comprising PM6/pentacene was then constructed, as shown in Fig. S19. The transfer curves obtained under both dark conditions and illumination with 520 nm light at an intensity of 1 mW/cm^2 illustrate an elevated I_{DS} within the device during illumination as compared to its dark state, demonstrating a positive photoresponse. This observation is attributed to the photo-generated electrons from PM6 being trapped by the PS, leaving excess holes and increasing the current. Subsequently, devices incorporating Y7-BO/pentacene were similarly constructed. As depicted in Fig. S20, the transfer curves observed under dark and light illumination with 830 nm at an intensity of 1 mW/cm^2 reveal that the device exhibits a negative photoresponse. This behavior arises from Y7-BO's pronounced electron-trapping capability. Consequently, holes generated under illumination transfer to pentacene due to potential energy barriers, leaving excess electrons within the Y7-BO layer. The device comprised of PM6/Y7-BO further substantiates the role of pentacene, as illustrated in Fig. S21. The transfer curves under both dark conditions and light illumination with 520 and 830 nm reveal that the device consistently displays a positive photoresponse during illumination. These results

indicate that the NPC behavior of the device is attributable to the photo-generated holes from the light-absorbing layer transitioning into the pentacene layer.

Employing the gate-tunable bidirectional photoresponse of our device to both visible and NIR light, we conducted a comprehensive simulation focusing on critical data processing, particularly highlighting edge detection, as depicted in Fig. 4d. The bidirectional modulation of visible light proves effective for detecting feature edges in bright environments. In contrast, bidirectional modulation of NIR light becomes essential in dark nighttime settings. The resulting photocurrent corresponds to a convolutional kernel, characterized by a 3 × 3 matrix configuration, as illustrated in Fig. 4e. The edge detection process systematically unfolds through the sequential convolutional interaction of individual input pixels with the kernel matrix. As demonstrated in Fig. 4f, our device enables precise edge detection for feature objects under both bright and dark conditions. Leveraging the device's broad spectral response and spatial gradient extraction enhances image information's spatial resolution and fidelity in complex lighting environments. The precision can reach 85 % under bright conditions and maintain a precision of 70 % even in dark conditions. Fig. S22 compares the edge extraction capabilities of devices without additives to those with 0.25 vol% additives. The additive-based device exhibits superior edge feature extraction ability due to the wider range of light conductance variation induced by light harvesting in the porous structure. The bidirectional photoresponse capabilities inherent to our device not only

underscore its intrinsic technological prowess but also facilitate the emulation and integration of edge computing preprocessing paradigms within visual imagery. This establishes its potential efficacy for visual data analytics and processing in varying lighting conditions.

Considering the device's ability to manifest PPC and NPC behaviors across diverse V_{GS} conditions, this device emerges as a promising candidate for critical data encryption. Consequently, a comprehensive investigation is undertaken to investigate the device's photoresponsive characteristics under continuous light pulses (1 mW/cm², $t_d = 0.5$ s, $\Delta t = 0.5$ s) at specific wavelengths of 450, 520, and 650 nm. As shown in Fig. 5a, under a reading voltage of 5 V, the device led a positive photoresponse for all three wavelengths and maintained a higher photocurrent level after 50 consecutive light pulses. Conversely, Fig. 5b exhibits the negative photocurrents of the device at a reading voltage of −5 V. To systematically evaluate the device's performance under different light pulses, a statistical overview of the variations in electrical conductivity for each wavelength is presented, as shown in Fig. 5c.

Based on the conductance values observed under different pulses and varying wavelengths, these values were quantified and utilized to enhance the security of visual information through RGB-based encryption. Specifically, conductance values were translated into pixel intensities and incorporated into grayscale images, embedding RGB noise within the images as shown in Fig. 5d. The encryption process primarily relies on the intensity of the light pulses rather than their specific wavelengths, ensuring that image information is obscured by the overall noise intensity, thereby creating a more robust cryptographic layer. Employing RGB light for encryption is crucial as it introduces a multi-dimensional noise pattern, significantly enhancing the complexity and security of the encrypted image. By integrating noise that varies with RGB intensities, the encryption becomes more intricate and less predictable. During encryption, with a V_{GS} of 5 V, the phototransistor array operates in PPC mode under visible light, encoding the image information based on light-induced conductance changes. This setup strengthens the encryption mechanism by directly embedding noise into
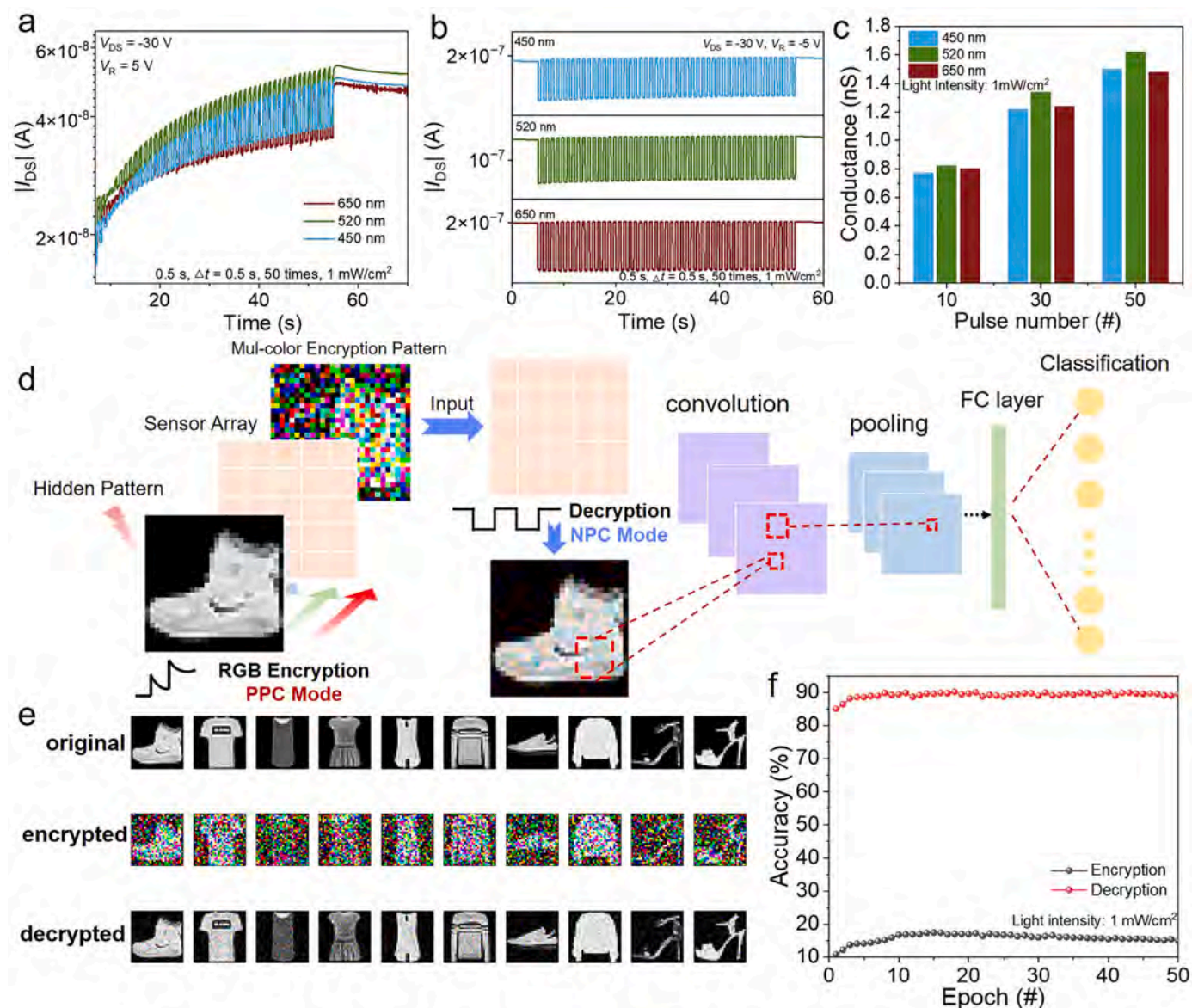

Fig. 5. (a) PPC and (b) NPC characteristics of the phototransistor with 0.25 vol% additives under 450, 520, and 650 nm light pulses and different reading voltages (pulse number: 50, t_d: 0.5 s, $\Delta t = 0.5$ s, pulse intensity = 1 mW/cm²). (c) Statistics of the positive photoconductance as a function of pulse number under different light pulses with wavelengths of 450, 520, and 650 nm. The light intensity was 1 mW/cm², and the duration and interval were both 0.5 s. (d) The image is encrypted and decrypted by the array by applying 50 light pulses of 450, 520, and 650 nm with $V_{GS} = \pm 5$ V, and the decrypted image is further classified and identified by the CNN network. (e) A comparison of images encrypted and decrypted by the array. (f) The recognition accuracy of images encrypted and decrypted by the array.

the visual information. For decryption, negative photoconductivity values are utilized with a reading voltage of −5 V. This negative photoconductance assists in reversing the encryption process by mapping these values back onto the corresponding pixels in the image, thus recovering the original image information. This decryption method effectively compensates for the noise introduced during encryption. The process was validated by encrypting 10 typical images from the Fashion MNIST dataset using the phototransistor array, as demonstrated in Fig. 5e. Using the conductance of 50 light pulses to encrypt the images, the particularly fuzzy images were obtained. The convolutional neural network (CNN) was further used to recognize the encrypted image, and the recognition accuracy was only 12 %, attesting to the effectiveness of the encryption process in concealing visual information. Fig. S23 illustrates the encryption strength of the image at three distinct levels based on the number of light pulses. We extracted the conductance values at 10, 30, and 50 light pulses to encrypt the image. It can be seen that as the number of pulses increases, the encryption effect of the pattern is better. It demonstrates that the phototransistor array can effectively serve an image encryption function. In stark contrast, the decrypted images demonstrated in Fig. 5e exhibit obvious original images with a recognition accuracy exceeding 90 %, affirming the device's exceptional capability in decryption operations. Fig. S24 and S25 depict the decryption of the image at three distinct levels under varying light intensities. When the light intensity is reduced to 0.25 mW/cm^2, the decryption effect of the phototransistor array on the image is illustrated in Fig. S24b. At this point, the decrypted image remains somewhat blurred, with only a 52 % recognition accuracy (Fig. S24c). With a light intensity of 0.5 mW/cm^2, the decrypted image achieves a recognition accuracy of 60 %. Fig. S26 exhibits the images encrypted and decrypted by the transistor without additives. However, devices without additives can still encrypt and decrypt image information. It can be seen from Fig. S27 that the device incorporating additives has better encryption and decryption effects, attributed to a larger range of conductivity changes. These results underscore the device's improvement in strong encryption and reliable decryption of visual information after introducing the porous structure.

3. Conclusion

The ternary organic heterostructure phototransistor was constructed for adaptive critical data processing. A three-dimensional porous photosensitive layer induced by the phase separation process enhances the light absorption power per unit volume by 2.5-fold. The device demonstrates a gate-tunable bidirectional photoresponse of non-volatile PPC and volatile NPC to visible and NIR light, enabling image edge detection in varying lighting conditions with precision above 85 %. The high-fidelity encryption and decryption processes were achieved by phototransistor array with superior accuracy of 12 %/90 %. This innovative ternary organic heterostructure device exemplifies efficient and compact processing capabilities for critical data.

4. Methods

4.1. Material preparation

PM6 (99 %, Mn 45k Da, Mw 97k Da, PDI = 2.16) and Y7-BO (98 %) were purchased from Nanjing Zhiyan Technology Co., Ltd. 1-chloronaphthalene (CN), 1,10-decanediol (DDO), polystyrene (MW: 35 w) and chloroform (CF) were purchased from Aladdin. Pentacene was purchased from J&K Scientific.

4.2. Device fabrication and measurement

The Si substrate was cleaned by ultrasonic treatment in acetone, ethyl alcohol and deionized water, for 10 min, respectively. Next, the Si substrate was treated 10 min under UV/ozone environment after drying

with nitrogen. PS solution (5 mg/mL in toluene) was spun-coated onto the Si substrate at 3000 rpm for 40 s and annealed at 100 ℃ for 30 min in glovebox with N$_2$ atmosphere. For the phototransistors based on additive-free BHJ, the concentration of PM6 and Y7-BO solution was 7.5 and 9 mg/mL in CF. PM6:Y7-BO solutions at volume ratio of 1:1 were spun onto the PS layer at 2000 rpm for 40 s and annealed at 100 ℃ for 10 min. For the device based on BHJ with additives, the CN was added in Y7-BO soluion with volume ratio of 0.1 vol%, 0.25 vol%, 0.5 vol%, and 1 vol% and DDO was added in PM6 solution with the same volume ratio. And then two solutions were mixed in a volume ratio of 1:1 and spun onto the PS layer at 2000 rpm for 40 s and annealed at 100 ℃ for 10 min. Finally, 40 nm pentacene and 40 nm Cu layer was then deposited as the top electrode under high vacuum (≈3 × 10^{-4} Pa). All electrical measurements were conducted using a Keithley 2636B semiconductor parameter analyzer under ambient conditions without any packaging. For all the phototransistors, illumination was performed with a xenon light Source.

4.3. Characterization

The morphologies of the BHJ and pentacene films were characterized by AFM (Bruker's Dimension Icon Atomic Force Microscopy). The UV–vis absorption spectra were obtained using a LAMBDA 35. GIWAXS measurement were carried out with a Xeuss 2.0 SAXS/WAXS laboratory beamline using a Cu X-ray source (8.05 keV, 1.54 Å) and a Pilatus3R 300 K detector. The samples for GIWAXS measurements are fabricated on silicon substrates using the same recipe for the devices.

4.4. 3D FDTD simulation for absorption profile calculation

Full wave electromagnetic simulation was performed using Lumerical FDTD simulation software (www.lumerical.com). The simulation structure was based on measured results of the actual device via AFM. The refractive indices of the mesoporous BHJ and BHJ/pentacene layers were taken from spectroscopic ellipsometry measurements. The plane wave source with a wavelength was impinged along the z-direction, and the periodic boundary conditions for x-y axis and the perfectly matched layer for z-axis were imposed on the unit-cell structure. Then, the absorbed power per unit volume (P_{abs}) was calculated using the relation of $P = -\frac{1}{2}\omega|E|^2 Im(\varepsilon)$ where ω is the angular frequency, E is the electric field, and Im(ε) is the imaginary part of the permittivity of perovskite material.

4.5. Image edge detection by transistor array

Firstly, the image was converted to grayscale, where pixel values were scaled to a range from 0 to 255 to standardize the intensity levels for uniform processing. This grayscale transformation ensures that each pixel's intensity is appropriately represented for subsequent analysis. Next, we configured the phototransistor array to perform image edge detection by programming it to apply a 3 × 3 convolutional kernel matrix. Specifically, we employed edge detection kernels such as the Sobel operators, which are commonly used for identifying horizontal and vertical edges. The Sobel operator matrices are $\begin{pmatrix} -1 & 0 & 1 \\ -2 & 0 & 2 \\ -1 & 0 & 1 \end{pmatrix}$ and $\begin{pmatrix} -1 & -2 & -1 \\ 0 & 0 & 0 \\ 1 & 2 & 1 \end{pmatrix}$ for horizontal and vertical edge detection. The phototransistor array was programmed to represent these kernel matrices. The array was then used to process different pixel values from the input grayscale image. Each phototransistor's responsivity (R) was measured under different gate reading voltage (−5, −10, 5, and 10 V), which reflects the convolution operation applied to the image. This measurement corresponds to a weighted average operation on the input image, where

the weights are determined by the convolutional kernel matrix. The output photocurrent thus represents the result of applying the 3×3 convolutional kernel to each pixel in the grayscale image, facilitating the edge detection process by highlighting regions of significant intensity change.

4.6. Image encryption and decryption

For image encryption, we employ a reading voltage of 5 V, which corresponds to the positive photoconductance state of the device. Initially, the conductance values of the device are mapped after it has been exposed to varying numbers of NIR light pulses. This mapping is based on the principle that the conductance of the device changes in response to the intensity and number of light pulses it receives, thereby encoding information related to the original image. Once the conductance values are mapped, we introduce Gaussian noise into the original image to encrypt it. This noise is proportionally added based on the conductance values of the device stimulated by RGB light under different numbers of pulses, relative to the initial conductance value of the device. Specifically, we calculate the ratios CR, CG, and CB, where: $C_R = \frac{\Delta G_R}{\Delta G_0}$, $C_G = \frac{\Delta G_G}{\Delta G_0}$, and $C_B = \frac{\Delta G_B}{\Delta G_0}$ is the initial conductance value of the device. These ratios dictate the level of Gaussian noise added to the image, effectively encoding the image with color-specific noise.

For image decryption, we use a reading voltage of -5 V, which corresponds to the negative photoconductance state of the device. Under this condition, the device's conductance is influenced by the RGB light intensities. We measure the ratio of the device's conductance variation after RGB light stimulation compared to the conductance variation when exposed to 1 mW/cm^2 of 830 nm light. This ratio serves as the denoising factor for decrypting the image. By adjusting the light intensities, we achieve different levels of denoising, which allows for the recovery of the original image based on the varying effects of light intensity on the device's conductance.

4.7. Image recognition based on CNN

The Convolutional Neural Network (CNN) utilized the Rectified Linear Unit (ReLU) activation function for all convolutional and fully connected layers, except for the final layer, where the Softmax function was employed. The CNN was optimized, and the parameters were set as follows: learning rate=0.001. Additionally, a training batch size of 64 was employed. The convolutional layers of the CNN were structured with the "same" padding to maintain consistent spatial dimensions between input and output feature maps.

CRediT authorship contribution statement

He Shao: Writing – review & editing, Writing – original draft, Investigation, Formal analysis. **Yu Ji:** Investigation, Formal analysis, Data curation. **Ruiheng Wang:** Validation, Data curation. **Jing Liu:** Formal analysis, Data curation. **Yueqing Li:** Formal analysis, Data curation. **Benxin Liu:** Formal analysis, Data curation. **Wen Li:** Writing – review & editing, Resources, Funding acquisition. **Yannan Xie:** Writing – review & editing, Resources, Funding acquisition. **Linghai Xie:** Writing – review & editing, Supervision, Investigation, Funding acquisition, Conceptualization. **Johnny C. Ho:** Writing – review & editing, Project administration, Funding acquisition. **Wei Huang:** Project administration, Funding acquisition. **Haifeng Ling:** Writing – review & editing, Supervision, Funding acquisition, Conceptualization.

Declaration of Competing Interest

The authors declare that they have no known competing financial interests or personal relationships that could have appeared to influence the work reported in this paper.

Data availability

Data will be made available on request.

Acknowledgements

Appendix A. Supporting information

Supplementary data associated with this article can be found in the online version at doi:10.1016/j.nanoen.2024.110133.

References

[1] C. Jin, W. Liu, Y. Xu, Y. Huang, Y. Nie, X. Shi, G. Zhang, P. He, J. Zhang, H. Cao, J. Sun, J. Yang, Artificial vision adaption mimicked by an optoelectrical In$_2$O$_3$ transistor array, Nano Lett. 22 (2022) 3372–3379.

[2] G. Feng, J. Jiang, Y. Li, D. Xie, B. Tian, Q. Wan, Flexible vertical photogating transistor network with an ultrashort channel for in-sensor visual nociceptor, Adv. Funct. Mater. 31 (2021) 2104327.

[3] Y. Gong, P. Xie, X. Xing, Z. Lv, T. Xie, S. Zhu, H.H. Hsu, Y. Zhou, S.T. Han, Bioinspired artificial visual system based on 2D WSe$_2$ synapse array, Adv. Funct. Mater. 33 (2023) 2303539.

[4] H. Shao, Y. Li, W. Yang, X. He, L. Wang, J. Fu, M. Fu, H. Ling, P. Gkoupidenis, F. Yan, L. Xie, W. Huang, A. Reconfigurable, Optoelectronic synaptic transistor with stable Zr-CsPbI(3) nanocrystals for visuomorphic computing, Adv. Mater. 35 (2023) 2208497.

[5] X. Zhu, C. Gao, Y. Ren, X. Zhang, E. Li, C. Wang, F. Yang, J. Wu, W. Hu, H. Chen, High-contrast bidirectional optoelectronic synapses based on 2D molecular crystal heterojunctions for motion detection, Adv. Mater. 35 (2023) 2301468.

[6] S. Seo, B. Kim, D. Kim, S. Park, T.R. Kim, J. Park, H. Jeong, S.O. Park, T. Park, H. Shin, M.S. Kim, Y.K. Choi, S. Choi, The gate injection-based field-effect synapse transistor with linear conductance update for online training, Nat. Commun. 13 (2022) 6431.

[7] Y. Zhou, J. Fu, Z. Chen, F. Zhuge, Y. Wang, J. Yan, S. Ma, L. Xu, H. Yuan, M. Chan, X. Miao, Y. He, Y. Chai, Computational event-driven vision sensors for in-sensor spiking neural networks, Nat. Electron. 6 (2023) 870–878.

[8] Y. Chen, Y. Kang, H. Hao, X. Xie, J. Zeng, T. Xu, C. Li, Y. Tan, L. Fang, All two-dimensional integration-type optoelectronic synapse mimicking visual attention mechanism for multi-target recognition, Adv. Funct. Mater. 33 (2022) 2209781.

[9] Z. Zhang, S. Wang, C. Liu, R. Xie, W. Hu, P. Zhou, All-in-one two-dimensional retinomorphic hardware device for motion detection and recognition, Nat. Nanotechnol. 17 (2022) 27–32.

[10] L. Sun, Y. Du, H. Yu, H. Wei, W. Xu, W. Xu, An artificial reflex arc that perceives afferent visual and tactile information and controls efferent muscular actions, Res. (Wash. D. C.) 2022 (2022) 9851843.

[11] J. Zhang, Y. Lu, S. Dai, R. Wang, D. Hao, S. Zhang, L. Xiong, J. Huang, Retina-inspired organic heterojunction-based optoelectronic synapses for artificial visual, Syst., Res. (Wash. D. C.) 2021 (2021) 7131895.

[12] C. Shi, J. Yang, N. Wu, Z. Wang, A high speed multi-level-parallel array processor for vision chips, Sci. China Inf. Sci. 57 (2014) 1–12.

[13] K. Kagawa, K. Yasuoka, D.C. Ng, T. Furumiya, T. Tokuda, J. Ohta, M. Nunoshita, Pulse-domain digital image processing for vision chips employing low-voltage operation in deep-submicrometer technologies, IEEE J. Sel. Top. Quantum Electron. 10 (2004) 816–828.

[14] W. Zhang, Q. Fu, N.-J. Wu, A programmable vision chip based on multiple levels of parallel processors, IEEE J. Solid-State Circuits 46 (2011) 2132–2147.

[15] G. Gallego, T. Delbruck, G. Orchard, C. Bartolozzi, B. Taba, A. Censi, S. Leutenegger, A.J. Davison, J. Conradt, K. Daniilidis, D. Scaramuzza, Event-based vision: a survey, IEEE Trans. Pattern Anal. Mach. Intell. 44 (2022) 154–180.

[16] Shunli Ma, Tianxiang Wu, Xinyu Chen, Yin Wang, Jingyi Ma, Honglei Chen, Antoine Riaud, Jing Wan, Zihan Xu, Lin Chen, Junyan Ren, David Wei Zhang, Peng Zhou*, Yang Chai*, W. Bao*, A 619-pixel machine vision enhancement chip based on two-dimensional semiconductors, Sci. Adv. (2022) eabn9328.

[17] A.P. Shunmugam, J.G. Fernandez, Characterization, manipulation, and isolation of Paramecium aurelia using a micro-electromigration chip and computer vision, Adv. Mater. Technol. 5 (2020) 2000152.

[18] J. Du, D. Xie, Q. Zhang, H. Zhong, F. Meng, X. Fu, Q. Sun, H. Ni, T. Li, E.-J. Guo, H. Guo, M. He, C. Wang, L. Gu, X. Xu, G. Zhang, G. Yang, K. Jin, C. Ge, A robust

neuromorphic vision sensor with optical control of ferroelectric switching, Nano Energy 89 (2021) 106439.

[19] S. Feng, J. Li, L. Feng, Z. Liu, J. Wang, C. Cui, O. Zhou, L. Deng, H. Xu, B. Leng, X. Q. Chen, X. Jiang, B. Liu, X. Zhang, Dual-mode conversion of photodetector and neuromorphic vision sensor via bias voltage regulation on a single device, Adv. Mater. 35 (2023) e2308090.

[20] A. Komar, R.A. Aoni, L. Xu, M. Rahmani, A.E. Miroshnichenko, D.N. Neshev, Edge detection with mie-resonant dielectric metasurfaces, ACS Photonics 8 (2021) 864–871.

[21] M.A. Kats, Two-dimensional optical edge detection, Nat. Photonics 14 (2020) 266–267.

[22] S. Lee, R. Peng, C. Wu, M. Li, Programmable black phosphorus image sensor for broadband optoelectronic edge computing, Nat. Commun. 13 (2022) 1485.

[23] A. Cao, S. Li, H. Chen, M. Deng, X. Xu, L. Shang, Y. Li, A. Cui, Z. Hu, A polar-switchable and controllable negative phototransistor for information encryption, Mater. Horiz. 10 (2023) 5099–5109.

[24] X. Bi, C. Shuai, B. Liu, B. Xiao, W. Li, X. Gao, Privacy-preserving color image feature extraction by quaternion discrete orthogonal moments, IEEE Trans. Inf. Forensics Secur. 17 (2022) 1655–1668.

[25] T. Yang, J. Ma, Y. Miao, X. Liu, X. Wang, B. Xiao, Q. Meng, Privacy-Preserving Krawtchouk Moment feature extraction over encrypted image data, Inf. Sci. 536 (2020) 244–262.

[26] H. Lai, Y. Zhou, H. Zhou, N. Zhang, X. Ding, P. Liu, X. Wang, W. Xie, Photoinduced multi-bit nonvolatile memory based on a van der Waals heterostructure with a 2D-perovskite floating gate, Adv. Mater. 34 (2022) e2110278.

[27] H. Jawa, A. Varghese, S. Ghosh, S. Sahoo, Y. Yin, N.V. Medhekar, S. Lodha, Wavelength-controlled photocurrent polarity switching in BP-MoS$_2$ heterostructure, Adv. Funct. Mater. 32 (2022) 2112696.

[28] X. Wang, L. Zhang, L. Hu, Z. Xie, H. Mao, L. Tan, Y. Zhang, Y. Chen, High-efficiency (16.93%) pseudo-planar heterojunction organic solar cells enabled by binary additives strategy, Adv. Funct. Mater. 31 (2021) 2102291.

[29] Y. Yan, X. Li, F. Zhang, M. Li, J. Zhou, T. Lin, Y. Zhu, D. Xu, Ternary organic solar cells with binary additives finely regulated active layer morphology and improved photovoltaic performance, Sol. RRL 7 (2023) 2300225.

[30] G. Sun, X. Jiang, X. Li, L. Meng, J. Zhang, S. Qin, X. Kong, J. Li, J. Xin, W. Ma, Y. Li, High performance polymerized small molecule acceptor by synergistic optimization on pi-bridge linker and side chain, Nat. Commun. 13 (2022) 5267.

[31] Z. Shen, J. Yu, G. Lu, K. Wu, Q. Wang, L. Bu, X. Liu, Y. Zhu, G. Lu, Surface crystallinity enhancement in organic solar cells induced by spinodal demixing of acceptors and additives, Energy Environ. Sci. 16 (2023) 2945–2956.

[32] K.S. Wienhold, V. Korstgens, S. Grott, X. Jiang, M. Schwartzkopf, S.V. Roth, P. Muller-Buschbaum, Effect of solvent additives on the morphology and device performance of printed nonfullerene acceptor based organic solar cells, ACS Appl. Mater. Interfaces 11 (2019) 42313–42321.

[33] F. Yang, H. Chen, R. Zhang, X. Liu, W. Zhang, J. Zhang, F. Gao, L. Wang, Efficient and spectrally stable blue perovskite light-emitting diodes based on potassium passivated nanocrystals, Adv. Funct. Mater. 30 (2020) 1908760.

[34] D. Li, L. Zhu, X. Liu, W. Xiao, J. Yang, R. Ma, L. Ding, F. Liu, C. Duan, M. Fahlman, Q. Bao, Enhanced and balanced charge transport boosting ternary solar cells over 17% efficiency, Adv. Mater. 32 (2020) e2002344.

[35] C.L. Radford, P.D. Mudiyanselage, A.L. Stevens, T.L. Kelly, Heteroatoms as rotational blocking groups for non-fullerene acceptors in indoor organic solar cells, ACS Energy Lett. 7 (2022) 1635–1641.

[36] R. Xiao, H. Yu, M. Liu, W. Xu, Y. Qin, R. Tan, Y. Chen, J. Wen, X. Peng, W. Gu, C. Zhu, L. Hu, Selective chemical reactivity of non-fullerene acceptor for photoelectrochemical bioassay of urease activity, Adv. Funct. Mater. 33 (2023) 2304915.

[37] Z. Abbas, S.U. Ryu, M. Haris, C.E. Song, H.K. Lee, S.K. Lee, W.S. Shin, T. Park, J.-C. Lee, Optimized vertical phase separation via systematic Y6 inner side-chain modulation for non-halogen solvent processed inverted organic solar cells, Nano Energy 101 (2022) 107574.

[38] Y. Wei, Y. Cai, X. Gu, G. Yao, Z. Fu, Y. Zhu, J. Yang, J. Dai, J. Zhang, X. Zhang, X. Hao, G. Lu, Z. Tang, Q. Peng, C. Zhang, H. Huang, Over 18% efficiency ternary organic solar cells with 300 nm thick active layer enabled by an oligomeric acceptor, Adv. Mater. 36 (2023) 2304225.

[39] M. Zhang, L. Zhu, T. Hao, G. Zhou, C. Qiu, Z. Zhao, N. Hartmann, B. Xiao, Y. Zou, W. Feng, H. Zhu, M. Zhang, Y. Zhang, Y. Li, T.P. Russell, F. Liu, High-efficiency organic photovoltaics using eutectic acceptor fibrils to achieve current amplification, Adv. Mater. 33 (2021) e2007177.

[40] X. Yang, B. Li, X. Zhang, S. Li, Q. Zhang, L. Yuan, D.H. Ko, W. Ma, J. Yuan, Intrinsic role of volatile solid additive in high-efficiency PM6:Y6 series nonfullerene solar cells, Adv. Mater. 35 (2023) e2301604.

[41] S. Liang, S. Li, Y. Zhang, T. Li, H. Zhou, F. Jin, C. Sheng, G. Ni, J. Yuan, W. Ma, H. Zhao, Efficient hole transfer via delocalized excited state in small molecular acceptor: a comparative study on photodynamics of PM6:Y6 and PM6:ITIC organic photovoltaic blends, Adv. Funct. Mater. 31 (2021) 2102764.

[42] S. Cheng, L. Wang, C. Guo, D. Li, J. Cai, W. Miao, B. Du, P. Wang, D. Liu, T. Wang, Reduced miscibility between highly compatible non-fullerene acceptor and donor enables efficient ternary organic solar cells, Polymer 236 (2021) 124322.

[43] J. Jo, S. Jeong, D. Lee, S. Lee, B.J. Kim, S. Cho, J.-Y. Lee, Pseudo-bilayered inverted organic solar cells using the Marangoni effect, J. Mater. Chem. A 11 (2023) 17307–17315.

[44] N. Tokmoldin, C. Deibel, D. Neher, S. Shoaee, Contemporary impedance analyses of archetypical PM6:Y6 bulk-heterojunction blend, Adv. Energy Mater. 14 (2024) 2401130.

[45] S.M. Kang, S. Jang, J.K. Lee, J. Yoon, D.E. Yoo, J.W. Lee, M. Choi, N.G. Park, Moth-Eye TiO$_2$ layer for improving light harvesting efficiency in perovskite solar cells, Small 12 (2016) 2443–2449.

[46] H. Yu, X. Zhao, M. Tan, B. Wang, M. Zhang, X. Wang, S. Guo, Y. Tong, Q. Tang, Y. Liu, Ultraflexible and ultrasensitive near-infrared organic phototransistors for hemispherical biomimetic eyes, Adv. Funct. Mater. 32 (2022) 2206765.

[47] X. Wu, C. Gao, Q. Chen, Y. Yan, G. Zhang, T. Guo, H. Chen, High-performance vertical field-effect organic photovoltaics, Nat. Commun. 14 (2023) 1579.

He Shao works as a postdoctoral fellow in Materials Science and Engineering at the City University of Hong Kong. She worked in the Institute of Advanced Materials (IAM), Nanjing University of Posts & Telecommunications (NJUPT) in 2021. She obtained her B.S. from the College of Physics, Jilin Normal University in 2016. In 2021, she obtained her Ph.D. from Jilin University. Her research interests focus on phototransistors, memristors, and synaptic devices.

Linghai Xie received the Ph.D. degree from the Institute of Advanced Materials (IAM), Fudan University in 2006, and then he worked in Nanjing University of Posts and Telecommunications (NUPT). He is currently a professor of materials chemistry and a director at the Center for Molecular Systems and Organic Devices (CMSOD). His research interest includes the molecular design of organic semiconductors by ecofriendly procedures, and their applications in organic devices and supramolecular optoelectronics.

Johnny C. Ho is a Professor of Materials Science and Engineering at the City University of Hong Kong. He received his B. S. degree in Chemical Engineering and his M.S. and Ph.D. degrees in Materials Science and Engineering from the University of California, Berkeley, in 2002, 2005, and 2009, respectively. From 2009–2010, he was a postdoctoral research fellow in the Nanoscale Synthesis and Characterization Group at Lawrence Livermore National Laboratory. His research interests focus on the synthesis, characterization, integration, and device applications of nanoscale materials for various technological applications, including nanoelectronics, sensors, and energy harvesting.

Haifeng Ling is a professor at Nanjing University of Posts and Telecommunications (NJUPT). He received his Ph.D. in organic electronics from NJUPT. Then he worked as a postdoctoral fellow at the Hong Kong Polytechnic University and an Alexander von Humboldt postdoctoral researcher at the Max Planck Institute for Polymer Research, respectively. In 2019, he joined the Institute of Advanced Materials (IAM) at NJUPT. His research interests focus on organic flexible neuromorphic electronics.